ICWMC 2025

The Eleventh International Conference on Wireless and Mobile Communications

ISBN: 978-1-68558-232-6

March 9th –13th, 2025

Lisbon, Portugal

ICWMC 2025 Editors

Dragana Krstic, University of Niš, Serbia

ICWMC 2025

Forward

The Twenty-First International Conference on Wireless and Mobile Communications (ICWMC 2025), held between March 9th, 2025, and March 13th, 2025, in Lisbon, Portugal, continued a series of international events on advanced wireless technologies, wireless networking, and wireless applications.

The event addressed wireless related topics concerning integration of latest technological advances to realize mobile and ubiquitous service environments for advanced applications and services in wireless networks. Mobility and wireless, special services and lessons learnt from particular deployment complemented the traditional wireless topics.

We take the opportunity to warmly thank all the members of the ICWMC 2025 technical program committee, as well as all the reviewers. The creation of such a high-quality conference program would not have been possible without their involvement. We also kindly thank all the authors who dedicated much of their time and effort to contribute to ICWMC 2025. We truly believe that, thanks to all these efforts, the final conference program consisted of top-quality contributions. We also thank the members of the ICWMC 2025 organizing committee for their help in handling the logistics of this event.

We hope that ICWMC 2025 was a successful international forum for the exchange of ideas and results between academia and industry for the promotion of progress in the field of wireless and mobile communications.

ICWMC 2025 Chairs

ICWMC 2025 Steering Committee
Dragana Krstic, University of Niš, Serbia
Rajat Kumar Kochhar, Ericsson, Sweden
Magnus Jonsson, Halmstad University, Sweden
Sonia Ben Rejeb, Higher Institute of Computer Science (ISI), University of Tunis El Manar (UTM), Tunisia

ICWMC 2025 Publicity Chairs
Francisco Javier Díaz Blasco, Universitat Politècnica de València, Spain
Ali Ahmad, Universitat Politècnica de València, Spain
José Miguel Jiménez, Universitat Politècnica de València, Spain
Sandra Viciano Tudela, Universitat Politècnica de València, Spain

ICWMC 2025
Committee

ICWMC 2025 Steering Committee

Dragana Krstic, University of Niš, Serbia
Rajat Kumar Kochhar, Ericsson, Sweden
Magnus Jonsson, Halmstad University, Sweden
Sonia Ben Rejeb, Higher Institute of Computer Science (ISI), University of Tunis El Manar (UTM), Tunisia

ICWMC 2025 Publicity Chairs

Francisco Javier Díaz Blasco, Universitat Politècnica de València, Spain
Ali Ahmad, Universitat Politècnica de València, Spain
José Miguel Jiménez, Universitat Politècnica de València, Spain
Sandra Viciano Tudela, Universitat Politècnica de València, Spain

ICWMC 2025 Technical Program Committee

Mohamed Abid, University of Gabes, Tunisia
Bedoui Abla, CEDOC-2IT | INPT (National Institute of Posts and Telecommunication), Morocco
Afrand Agah, West Chester University of Pennsylvania, USA
Iness Ahriz, CNAM, France
Khalil Aissaoui, Tunisia Polytechnic School (TPS), Tunisia
Wafa Akkari, University of Manouba, Tunisia
Ali Kadhum M. Al-Quraby, University of Babylon, Iraq
Diego Alberto Godoy, Universidad Gastón Dachary, Argentina
Adel Aldalbahi, King Faisal University, Saudi Arabia
Farman Ali, Qurtuba University of Science and IT, D.I. Khan, Pakistan
Adda Ali-Pacha, University of Sciences and Technology of Oran, Algeria
Firas Alsehly, Huawei Edinburgh Research Centre, UK
Karine Amis, IMT Atlantique, France
Tran Hai Anh, Hanoi University of Science and Technology (HUST), Vietnam
Antonio Arena, University of Pisa, Italy
Kamran Arshad, Ajman University, UAE
Nebojša Bačanin-Džakula, Singidunum University, Serbia
Salih Safa Bacanli, University of Central Florida, USA
Nedia Badri, ENSI - University of Manouba, Tunisia
Corey E. Baker, University of Kentucky, USA
Chaity Banerjee, University of Central Florida, USA
Kamel Barkaoui, Cedric | Cnam, France
Dimitri Belli, National Research Council (CNR) - Institute of Information Science and Technologies (ISTI), Pisa, Italy
Hadda Ben Elhadj, SM@RTS | Higher Institute of Informatics | Monastir University, Tunisia
Sonia Ben Rejeb, Higher Institute of Computer Science (ISI) - Higher School of Communications of Tunis (SUPCOM), Tunisia
Emna Ben Slimane, ENIT - Tunis El Manar University, Tunisia

Copyright Information

For your reference, this is the text governing the copyright release for material published by IARIA.

The copyright release is a transfer of publication rights, which allows IARIA and its partners to drive the dissemination of the published material. This allows IARIA to give articles increased visibility via distribution, inclusion in libraries, and arrangements for submission to indexes.

I, the undersigned, declare that the article is original, and that I represent the authors of this article in the copyright release matters. If this work has been done as work-for-hire, I have obtained all necessary clearances to execute a copyright release. I hereby irrevocably transfer exclusive copyright for this material to IARIA. I give IARIA permission or reproduce the work in any media format such as, but not limited to, print, digital, or electronic. I give IARIA permission to distribute the materials without restriction to any institutions or individuals. I give IARIA permission to submit the work for inclusion in article repositories as IARIA sees fit.

I, the undersigned, declare that to the best of my knowledge, the article is does not contain libelous or otherwise unlawful contents or invading the right of privacy or infringing on a proprietary right.

Following the copyright release, any circulated version of the article must bear the copyright notice and any header and footer information that IARIA applies to the published article.

IARIA grants royalty-free permission to the authors to disseminate the work, under the above provisions, for any academic, commercial, or industrial use. IARIA grants royalty-free permission to any individuals or institutions to make the article available electronically, online, or in print.

IARIA acknowledges that rights to any algorithm, process, procedure, apparatus, or articles of manufacture remain with the authors and their employers.

I, the undersigned, understand that IARIA will not be liable, in contract, tort (including, without limitation, negligence), pre-contract or other representations (other than fraudulent misrepresentations) or otherwise in connection with the publication of my work.

Exception to the above is made for work-for-hire performed while employed by the government. In that case, copyright to the material remains with the said government. The rightful owners (authors and government entity) grant unlimited and unrestricted permission to IARIA, IARIA's contractors, and IARIA's partners to further distribute the work.

Table of Contents

A Study on Realizing Start Frame Delimiter-Less Communication Using Reed-Solomon Codes

Deyuku Maeda, Naoki Morita
Tokai University Graduate School
School of Information and Telecommunication Engineering
Tokyo, Japan
e-mail: {2cjnm018, morita} @tokai.ac.jp

Kenta Morita
Faculty of Medical Engineering Dept.
Suzuka University of Medical Science
Mie, Japan
e-mail: morita@tsuzuka-u.ac.jp

***Abstract*—In communication systems, accurately identifying the transmitted data requires precise acquisition of the data reading position. The current packet extraction method, which uses a Start Frame Delimiter (SFD), suffers from poor noise resistance, leading to synchronization errors. To address this issue, this study proposes a novel packet extraction method that eliminates the use of SFD. By combining Reed-Solomon (RS) codes with a bit-shifting method, the proposed approach leverages the error-correcting capability of RS codes to identify packets even when bit reading positions are misaligned. Simulation results demonstrate that the proposed method achieves zero packet loss and effectively resolves the synchronization problem.**

Keywords-Frame synchronization; Start Frame Delimiter; Telecommunications; Reed-Solomon.

I. INTRODUCTION

Frame synchronization is particularly critical for packet transmission in cognitive radio networks [1]. The Start Frame Delimiter (SFD) is a key element in frame synchronization. Frame synchronization is achieved by the transmitter appending an SFD to the beginning of the transmitted data frame. The receiver detects the SFD to confirm the arrival of a packet and removes it from the data stream to reconstruct the transmitted message. Thus, the SFD plays a central role in frame synchronization. However, a significant issue arises due to noise superimposed on the SFD, leading to synchronization failures. This issue, known as "frame synchronization loss," becomes particularly problematic when the SFD is falsely detected, potentially causing delays in resynchronization. Frame synchronization loss directly impacts the overall reliability of communication systems, as has been previously demonstrated [2]. Therefore, solutions to further reduce its occurrence are critically needed. Optimizing the SFD design alone has proven insufficient to fully eliminate frame synchronization errors. Consequently, this study aims to address the root cause by proposing a communication algorithm that eliminates the dependency on the SFD altogether. The structure of this paper is as follows: Section II provides an overview of related works on SFD design using Barker codes. Section III explains the objectives and methodology of this research. Section IV presents the simulation settings, results, and discussions. Finally, Section V summarizes the findings and outlines future research directions.

II. RELATED WORK

Approaches to address the issue of frame synchronization loss have included simulation-based performance evaluations of recovery time [2] and methods involving changes to frame length [3]. However, the primary cause of frame synchronization loss lies in the Start Frame Delimiter (SFD), making its design a critical approach. One such approach involves using Barker codes for SFD design. Barker code sequences function as known reference signals for frame synchronization and are known for their excellent autocorrelation properties [4]. Cuji et al. [5] implemented a frame detection algorithm based on the autocorrelation properties of Barker sequences in a digital communication system, comparing simulation results with those obtained in real wireless link environments. These studies confirmed the effectiveness of Barker codes in SFD design and their contribution to improving synchronization accuracy. We further evaluated various SFD patterns (primarily Barker codes) under different noise conditions to examine their impact on synchronization errors. The results showed that shorter SFD patterns, such as "1110," were the most effective in minimizing synchronization errors while maintaining a high success rate. While successfully identified the optimal SFD, synchronization errors have not been entirely eliminated. Thus, further research is needed to explore alternative methods to reduce synchronization loss [6]. We propose a novel communication method that eliminates the use of the SFD, which is the root cause of synchronization errors. This approach aims to fundamentally resolve the limitations of traditional synchronization methods.

III. METHODOLOGY

This section outlines the objectives of this study and the methodologies employed. In this research, a method is proposed to extract only the bit sequences corresponding to packets from the entire received bit sequence. As shown in Figure 1, if the reading position of the bit sequence is misaligned, the interpretation of the data is entirely altered. Therefore, accurately determining the reading position is essential to identify the valid portions of the data. Since even a single-bit misalignment renders the bit sequence meaningless, precise identification of the packet position is indispensable. To achieve this, the proposed method employs coding techniques. Encoded data cannot be correctly decoded

unless it is read from the correct position. Figure 1 illustrates an example where bit misalignment causes all information to change, emphasizing the importance of proper decoding at the correct position. In the proposed method, bit shifting is performed on the received bit sequence based on the fixed length of the code, and decoding is attempted. The position where decoding succeeds is identified as the packet and extracted accordingly. Reed-Solomon codes, with a parameter (t = (N-K) / 2), can correct up to t symbol errors, where tt is the maximum number of correctable symbol errors, N is the total number of symbols in a codeword, and K is the number of plaintext symbols. Leveraging this property, completely unrelated bit sequences can be discarded, as they inherently contain more errors than RS codes can correct. Conversely, valid bit sequences can be successfully decoded as long as they contain no more than (t) symbol errors. Furthermore, unrelated bit sequences inevitably result in decoding failures because they contain (t) or more symbol errors. This characteristic enables accurate packet extraction.

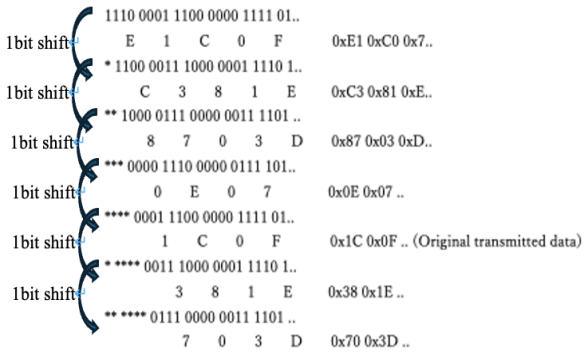

Fig. 1. Flowchart of the proposed method.

IV. SIMULATION

This section presents the simulation setup and results.

A *Simulation setup*

The outline of the simulation is as follows. The packet frame consists of a randomly generated data section, and the data section is protected by Forward Error Correction (FEC). Symbol length (n) and error correction capability (t) can be set arbitrarily. The transmission channel is modeled as an Additive White Gaussian Noise (AWGN) channel. The simulation involves sending 1000 packets, with each packet having a data section of 255 bytes. The idling period signal is always set to high, meaning the digital value 1.

B *Result and Consideration*

Figures 2 and 3 show the simulation results for varying code lengths of the Reed-Solomon (RS) code. It was revealed that both RS (128, 32) and RS (9, 3) achieve zero packet loss within the Bit Error Rate (BER) range that falls within the error-correction capability of the Reed-Solomon code. These results demonstrate the effectiveness of the proposed method. However, it was also observed that, on rare occasions, extra packets were erroneously extracted from incorrect positions.

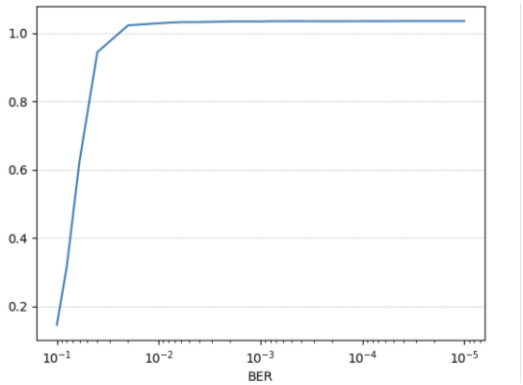

Fig. 2. Packet Extraction Rate RS (128, 32).

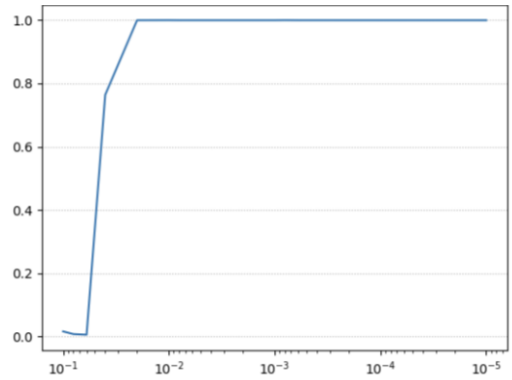

Fig. 3. Packet Extraction Rate RS (9, 3).

V. CONCLUSION AND FUTURE WORK

This study proposes a novel synchronization method that does not rely on the Start Frame Delimiter (SFD) to address the issue of synchronization errors. While previous studies have identified optimal SFDs, the problem of frame synchronization errors has not been completely resolved. In this research, a packet extraction method independent of SFD is proposed by extracting decodable sections as packets. Simulation results demonstrate the feasibility of the proposed synchronization method. However, a remaining challenge is the need for measures to address the rare occurrence of erroneously extracted packets from incorrect positions.

REFERENCES

[1] R. A. Scholtz, “Frame synchronization techniques,” IEEE Trans. Commun., vol. COM-28, no. 8, pp. 1204–1213, Aug. 1980.

[2] K. Makino, “Frame synchronization characteristics evaluation for code errors”, IEICE General Conference, 1996.

[3] W. Suwansantisuk, “Frame Synchronization for Variable-Length Packets”, IEEE Journal on Selected Areas in Communications, vol. 26, no. 1, January 2008.

[4] K.-U. Schmidt and J. Willms, “Barker sequences of odd length,” *[arXiv:1501.06035v1]*, January, 2015.

[5] D. D. A. Cuji, P. A. Chasi, F. Guerrero, and F. Rivera, “Frame synchronization through barker codes using SDRs in a real wireless link”, 2016 International Conference on Electronics, Communications and Computers, 2016.

[6] D. Maeda and M. Naoki, “Reducing Frame Synchronization Loss through Optimized Start Frame Delimiter”, WIRELESS ANALYTICS 2024.

Reinforcement Learning Based Goodput Maximization with Quantized Feedback in URLLC

Hasan Basri Celebi[1,2] and Mikael Skoglund[1]
[1]*KTH Royal Institute of Technology, Stockholm, Sweden*
[2]*Hitachi Energy, Västerås, Sweden*
e-mail: hasan-basri.celebi@hitachienergy.com, skoglund@kth.se

***Abstract*—This paper presents a comprehensive system model for goodput maximization with quantized feedback in Ultra-Reliable Low-Latency Communication (URLLC), focusing on dynamic channel conditions and feedback schemes. The study investigates a communication system, where the receiver provides quantized channel state information to the transmitter. The system adapts its feedback scheme based on reinforcement learning, aiming to maximize goodput while accommodating varying channel statistics. We introduce a novel Rician-K factor estimation technique to enable the communication system to optimize the feedback scheme. This dynamic approach increases the overall performance, making it well-suited for practical URLLC applications where channel statistics vary over time.**

Keywords-URLLC, reinforcement learning, quantized feedback, Rician-K estimation, goodput maximization.

I. Introduction

Ultra-Reliable Low-Latency Communication (URLLC) systems are facing the challenge of achieving reliability with maximum data transmission rates while dynamically responding to fluctuating channel conditions. In this context, goodput, which represents the rate of successful information transmission, is a key metric for evaluating overall system performance. Optimizing goodput emphasizes the significance of feedback mechanisms. These mechanisms let the transmitter adapt its transmission strategies efficiently [1].

A. Related Work

Various research explored scenarios where partial Channel State Information (CSI) is available, aiming to reduce system overhead compared to full feedback approaches. In [2], a more systematic feedback approach is explored, focusing on quantized CSI. Kim et al. [3] investigate wireless communication systems with partial CSI transmitted over an error-free quantized feedback channel in the asymptotic regime, proposing an adaptive feedback scheme to maximize goodput. Recently, advancements in finite blocklength regime for low-latency communication applications have been studied in [4].

On the other hand, significant advancements in URLLC with feedback systems have been highlighted in recent years. [5] addresses URLLC downlink transmission quality challenges ensuring reliability and flexibility in feedback transmission. Authors in [6] introduce Deep-HARQ, an AI-driven algorithm optimizing the interface design for URLLC, significantly reducing link latency. Furthermore, enhancements in downlink link adaptation for URLLC to improve the channel quality while enhancing system-level performance are presented in [7]. These contributions mark significant advancements in reliable URLLC systems with feedback mechanisms [8].

B. Motivation and Contributions

In this study, we assume a quasi-static fading channel where the channel coefficient h remains constant during transmission but varies over different codewords. One of the primary performance metrics in quasi-static fading channels is the system's overall goodput, which can be assessed by the expected rate achieved across a substantial number of packet transmissions with varying transmission rates. This scenario requires a feedback mechanism to transmit the current CSI to the transmitter. Therefore, we propose a system model that investigates the optimum quantized feedback scheme with the purpose of maximizing the overall goodput of the communication system. To extend the existing research, it is also assumed that the channel statistics vary over time due to factors such as mobility and scattering. For this purpose, a Rician distributed channel model is taken into account with an unknown shape factor, which will be defined in the next section.

The foundation of the proposed study lies in a two-part system. The contributions in the current paper can be listed as

- First, we introduce a novel technique for estimating the Rician-K factor, which characterizes the channel's shape factor. This estimate serves as a key input for the second part, where Reinforcement Learning (RL)-based strategies for quantized feedback scheme selection are applied.
- In the second part, we propose a novel RL-based search algorithm to design an adaptive feedback scheme. RL offers a flexible approach to learning and adapting to varying communication environments.

Our approach enables transceivers to dynamically adapt feedback strategies to current channel conditions, thereby maximizing goodput. This model offers a practical solution for dynamic channel adaptation which is crucial for evolving wireless technologies and the increasing demand in next-generation industrial communications for URLLC in the upcoming beyond-5G era.

The remainder of the paper is organized as follows: Section II details the system model and the definition of the problem, considering the varying channel statistics. Section III introduces our novel learning-based Rician-K factor estimator. In Section IV, we present and review the RL-based quantized feedback scheme. Section V provides a performance evaluation of the proposed system, and Section VI concludes the paper.

II. System Model

We consider the discrete-time complex baseband wireless communication system in which the transmitter transmits a codeword over a quasi-static fading channel, where the

complex-valued channel coefficient h is an independent and identically distributed (i.i.d.) random variable according to some distribution but remains constant over the codeword transmission. For the sake of the focus of the study, it is assumed that the receiver has perfect knowledge of h and transmits this information back to the transmitter via an error-free quantized feedback channel.

In such a communication environment, the received signal $\boldsymbol{y}$ can be expressed as

$$\boldsymbol{y} = h\boldsymbol{x} + \boldsymbol{z}, \tag{1}$$

where $\boldsymbol{x}$ and $\boldsymbol{z}$ represent the transmitted codeword and complex Gaussian noise vector where the samples are i.i.d. and $z_i \sim CN(0,1)$, where z_i represents the ith component of $\boldsymbol{z}$.

Let γ denote the i.i.d. channel magnitude which is determined as $\gamma = |h|$, where γ can be defined as a continuous random variable with its corresponding Probability Density Function (PDF), $p(\gamma)$, and Cumulative Distribution Function (CDF), $P(\gamma)$. In this study, it is assumed that both $p(\gamma)$ and $P(\gamma)$ are continuous and $p(\gamma) \geq 0$ over $0 \leq \gamma \leq \infty$.

A. Feedback Channel

It is considered that the receiver divides the positive real line into Λ number of quantization regions and applies a deterministic index mapping on the channel magnitude γ

$$L(\gamma) = l \text{ for } \gamma \in [\lambda_l, \lambda_{l+1}), \tag{2}$$

where $l = 0, 1, \cdots, \Lambda-1$ and $\lambda_0 = 0$ and $\lambda_\Lambda = \infty$. Afterward, the selected index, l, is transmitted back to the transmitter over the error-free feedback channel. Therefore, CSI is partially known to the transmitter.

After receiving the partial CSI, the transmitter selects a transmission rate, described as r_l, which can be defined as the selected rate for the lth quantized region, with the mission of maximizing the goodput of the communication system, which is the maximization of the overall correctly received information rate. For instance, the goodput of a communication system with constant transmission rate r and error rate ϵ is

$$G = r(1-\epsilon). \tag{3}$$

B. Problem Definition

The instantaneous channel capacity, for a given channel magnitude γ with SNR $\mathcal{P}$, is

$$C(\gamma) = \log(1+\gamma^2\mathcal{P}). \tag{4}$$

Suppose $\Lambda = \infty$, which represents perfect CSI at the transmitter, the maximum achievable goodput is the ergodic capacity since it is possible to match the transmission rate to $C(\gamma)$. Thus,

$$G_{\Lambda=\infty} = \int_0^\infty p(\gamma)C(\gamma)\mathrm{d}\gamma. \tag{5}$$

On the other hand, if $\Lambda = 1$, which means no CSI at the transmitter, the maximum achievable goodput can be found by solving the following optimization problem

$$G_{\Lambda=1} = \max_{r\geq 0} \int_{\sqrt{\frac{2^r-1}{\mathcal{P}}}}^\infty r p(\gamma)\mathrm{d}\gamma. \tag{6}$$

When $\Lambda \in [2, \infty)$, determining the maximum achievable goodput value becomes a challenging task. Consequently, the objective becomes identifying the optimal λ_l and r_l configurations that maximize the long-term goodput.

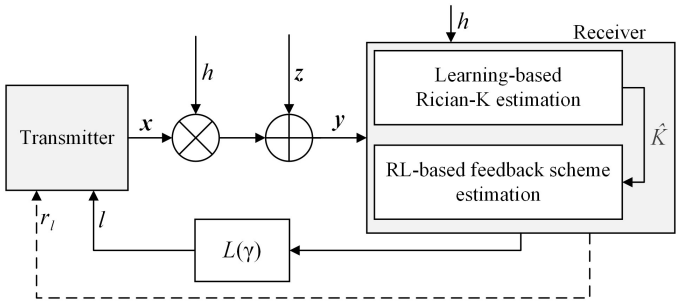

Figure 1. The proposed system model.

Suppose γ_l^r is the reconstruction point of the lth quantization region and the transmitter selects $r_l^r = C(\gamma_l^r)$ as the transmission rate. For a given channel realization γ, where $\lambda_l \leq \gamma < \lambda_{l+1}$, we know that as long as

$$r_l^r \leq \log(1+\gamma^2\mathcal{P}) = C(\gamma), \tag{7}$$

error-free transmission is possible. Otherwise, the communication is in outage. Thus, once the γ_l^rs and r_l^rs for $l = 1, 2, \cdots, \Lambda$ are estimated, the overall outage probability of such a communication system is

$$\sum_{l=0}^{\Lambda-1} (P(\gamma_l^r) - P(\lambda_l)). \tag{8}$$

Therefore, the optimum selections of λ_ls and r_ls can be found by solving the following optimization problem

$$\max_{r_l^r, \lambda_l, \gamma_l^r} \quad \sum_{l=0}^{\Lambda-1} r_l^r \left(P(\lambda_{l+1}) - P(\gamma_l^r)\right) \tag{9a}$$

$$\text{s.t.} \quad 0 < \lambda_l \leq \gamma_l^r < \lambda_{l+1} < \infty. \tag{9b}$$

This problem has been studied in [3], [4], and [9], and it was shown that optimum r_l^rs can be achieved by setting $r_l^r = C(\lambda_l)$ and quantization levels, λ_l^r for $l = 1, 2, \cdots, \Lambda-1$, can be found by solving the following equation with an iterative algorithm

$$P(\lambda_{l+1}^r) = P(\lambda_l^r) + \left(\frac{1}{\mathcal{P}} + \lambda_l^r\right) p(\lambda_l^r) \log\left(\frac{1+\lambda_l^r\mathcal{P}}{1+\lambda_{l-1}^r\mathcal{P}}\right). \tag{10}$$

C. Varying Channel Statistics

Notice that the channel statistics are assumed to be fixed in the optimization problem above. In this paper, we extend these results by *letting the channel statistics vary over time*.

It is assumed that $h \sim CN(\mu, \sigma^2)$, with slowly varying μ over time. Since $h \sim CN(\mu, \sigma^2)$, the channel magnitude, γ, is Rician distributed random variable with varying K-factor, which represents the shape parameter of the distribution and can be defined as the power ratio of the line-of-sight signal power to the remaining multipath and is expressed as [10]

$$K = \mu^2/\sigma^2. \tag{11}$$

This assumption is broader and more realistic for many real-world applications where the channel statistics change due to mobility, scattering, etc. In our analyses, we assumed that μ remains constant for 200 channel realizations and then changes to a new value.

For this purpose, we divide the proposed method into two parts: i) Rician-K factor estimation and ii) RL-based quantized feedback scheme selection. In the first part, we introduce a novel technique for estimating the Rician-K factor. The estimate obtained in this initial phase serves as an input for the subsequent part, where an RL-based strategy is employed to dynamically select and update the feedback scheme to optimize the overall goodput of the communication system, aligning it with the current channel statistics. The proposed system model is shown in Fig. 1.

In Fig. 1, it is worth highlighting the presence of two distinct feedback channels. The first feedback channel, depicted with a solid line, serves as the quantized feedback channel and is utilized in each transmission of a codeword. In contrast, the second feedback channel, indicated by a dashed line, plays a unique role during the training phase, specifically for transmitting updated transmission rates associated with quantization level l. It is important to emphasize that this secondary feedback channel is not employed in every subsequent transmission; rather, its usage is triggered by the decision made by the RL-based feedback scheme to update r_l, as will be discussed in Section IV. In this way, the transmitter's knowledge is restricted to the selected transmission rate r_l for each l, which minimizes the need for additional data transmission during training since all learning algorithms are implemented at the receiver. This also contributes to reducing the overall computational load on transceivers, which is a crucial factor for mitigating the latency due to computational processes [11] and [12].

III. Learning-Based Estimator for Rician-K Factor

Rician-K factor estimation is a well-studied topic in the literature. Moment-based and maximum-likelihood estimators have been presented in [10], [13]. Here, we first introduce the moment-based estimators and then present our findings.

The PDF of the channel magnitude γ is given by

$$p(\gamma) = \frac{2\gamma}{\sigma^2} \exp\Big(\frac{-(\gamma^2+\mu^2)}{\sigma^2}\Big) \mathrm{I}_0\Big(\frac{2\gamma\mu}{\sigma^2}\Big), \tag{12}$$

where $\mathrm{I}_z(\cdot)$ is the modified Bessel function of the first kind with order z. By using the first few raw moments of Rician distribution [14], the following estimators can be found after some straightforward mathematical steps

$$\frac{m_1}{\sqrt{m_2}} = \frac{1}{2}\sqrt{\frac{\pi}{K+1}} L_{\frac{1}{2}}(K), \tag{13}$$

$$\frac{m_4}{m_2^2} = 1 + \frac{(2K+1)}{(K+1)^2}, \tag{14}$$

$$\frac{m_6}{m_2^3} = 6 + \frac{K^2(5K-9)}{(K+1)^3}, \tag{15}$$

where $L_{\frac{1}{2}}(K)$ is the Laguerre polynomial, defined as

$$L_{\frac{1}{2}}(K) = \exp\left(-\frac{K}{2}\right)\left((K+1)\mathrm{I}_0\left(\frac{K}{2}\right) + K\mathrm{I}_1\left(\frac{K}{2}\right)\right), \tag{16}$$

and m_i represents the ith raw moment. By using the estimators above, an estimate of K is obtained numerically by computing the empirical moments and solving the nonlinear equations presented, where a close approximation for the Laguerre polynomial can also be used as in [15].

In this study, we extend these results and propose a novel moment-based learning model for Rician-K estimation. In this proposed method, we employ a more comprehensive set of features unlike the already presented studies in the literature [16], which uses the traditional amplitude samples directly. Specifically, we extract the first ten empirical moments of the Rice-distributed random variable as input features. These moments include the empirical mean, variance, skewness, and kurtosis.

The idea behind using these moments as input features is because of their ability to capture the underlying statistical characteristics of the Rician random variable γ. This approach offers a more detailed and informative representation of the channel compared to conventional moment-based estimators, which often rely only on a few moments. Our learning-based approach is based on the eXtreme-Gradient-Boosting (XGBoost) regression model, which has gained popularity in various domains for its capability to handle complex relationships with high-performance predictions [17]. Other learning algorithms such as linear regression, histogram-based gradient boosting regression, random forest regressor, cat-boost regressor, etc. are also investigated. We skipped their results since their overall performance was worse than XGBoost.

A. Pre-processing

Notice that the number of inputs of the proposed learning-based method does not change with the number of samples collected, which makes the proposed method easily scalable. On the other hand, identifying the number of samples, N, while computing the empirical raw moments becomes a significant design problem. To find the best selection, we have tested various N values and saw that the best performance is obtained when the training dataset is comprised of $N = 100$. However, similar performance results can be achieved with selections of $N > 50$ since XGBoost uses a learning rate to control the model's parameter updates during training [18], which aims to prevent overfitting while maintaining a low bias and ensuring that the model generalizes well to unseen data.

B. Performance Comparison

To test the performance of the proposed method, we resorted to Monte Carlo simulations and compared the results. For this purpose, a training dataset comprising 10^5 Rician-K factors is created. This dataset contains a range of K values, limited within $0 \leq K \leq 100$, and was appended with their respective empirical raw moments, which were computed from randomly generated samples, with each dataset comprising $N = 100$ samples. Even though we set a constant N for the training dataset, we test the performance of the learning-based estimator with various N values, which are $N = \{25, 50, 10^2, 10^3\}$. On the other hand, we select the estimator formulated in (13) as the moment-based estimator due to its leading performance against (14) and (15) since it uses the advantage of the lower order moments [10].

A comparison of the results is presented in Fig. 2, where the sample mean of the predicted K values, $\hat{K}$, are depicted with upper and lower limits of the confidence region, which is

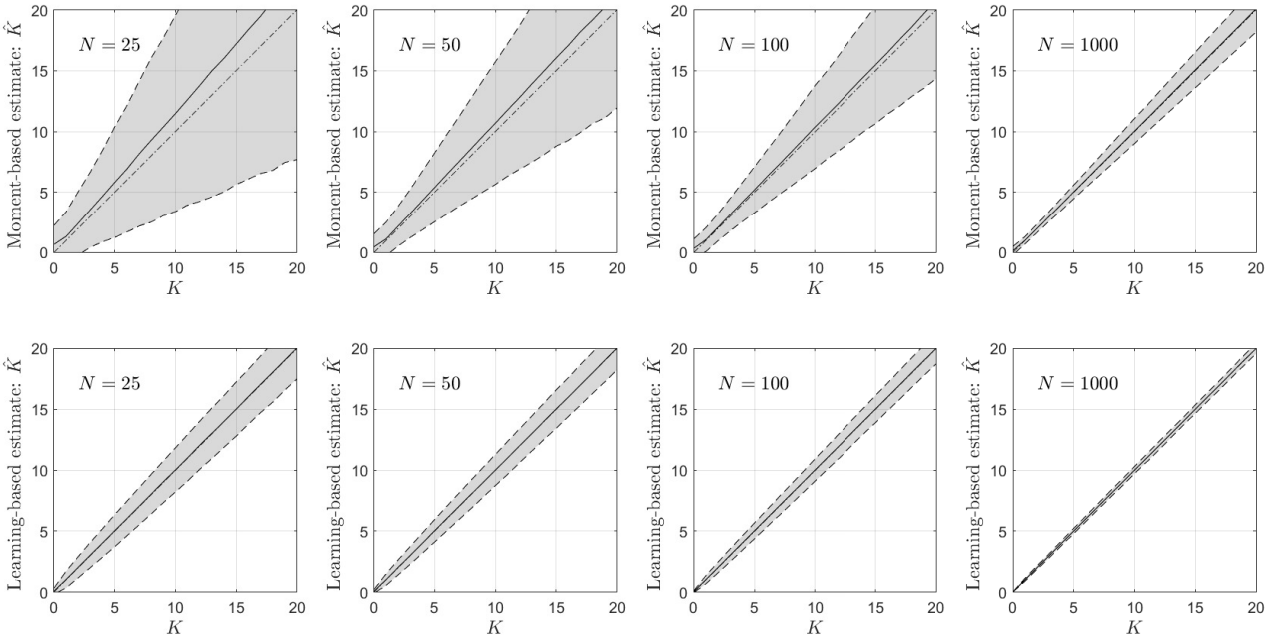

Figure 2. Sample mean and sample confidence region of the two estimators, namely moment-based and learning-based estimators. Results have been depicted for $N = \{25, 50, 100, 1000\}$. (——) Sample mean. (- - -) Upper and lower limits of the confidence region. (—·—) Reference line.

calculated as the $\pm 2\times$standard deviation of $\hat{K}$. Although the estimators are capable of detecting higher K values, we limit the horizontal and vertical axes between $[0 - 20]$ to have a better look at the differences between the estimators.

The key observation derived from Fig. 2 is the remarkable superiority of the learning-based estimator in comparison to the moment-based estimator across all choices of N. Interestingly, the learning-based estimator exhibits better performance, even at $N = 25$, compared to the moment-based estimator's results at $N = 10^2$. Furthermore, the learning-based estimator achieves nearly perfect estimations when $N = 10^3$.

IV. Reinforcement-Learning Based Quantized Feedback Scheme Selection

In this section, we focus on finding the optimum feedback scheme, such as selecting the best λ_ls and r_ls, to maximize the overall goodput of the system. As mentioned in the previous chapter, we use an RL-based search algorithm since the proposed methods in the literature cannot adapt to variable channel statistics.

Let us first denote the optimum selections as λ_l^* and r_l^*. It is shown in [3] that the optimum goodput is achieved by assigning the $r_l^* = C(\lambda_l^*)$. Thus, one can simplify the optimization problem by omitting the r_l variables. Next is the discritization process of the quantization regions. For this purpose, we define a finite number of values for λ_ls and reformulate the optimization problem in (9) as

$$\max_{\lambda_l, \gamma_l} \quad \sum_{l=1}^{\Lambda-1} r_l \big(P(\lambda_{l+1}) - P(\gamma_l)\big) \tag{17a}$$

$$\text{s.t.} \quad 0 \leq \lambda_l \leq \gamma_l < \lambda_{l+1} < \infty, \tag{17b}$$

$$\lambda_l \in \mathcal{S}, \tag{17c}$$

where $\mathcal{S}$ represents the set of finite number of selections. With this reformulation, the solution becomes a sequential search and can be modeled as a Markov decision process and therefore can be solved with RL [19].

A Markov decision process consists of four elements, such as the environment, state space $\mathcal{S}$, action space $\mathcal{A}$, and reward space Ω. In more detail, at each time step t (or at each iteration) the process is in state $s_t \in \mathcal{S}$ and makes a decision and chooses an action $a_t \in \mathcal{A}$. A reward $\omega_t \in \Omega$ is observed after taking the action. Thus, ω_t is received from the environment and is based on s_t and a_t.

For the reformulated optimization problem in (17), states, actions and rewards are designed as follows:

- *State space* $\mathcal{S}$: We set λ_ls for $l = \{1, 2, \cdots, \Lambda - 1\}$ as the agents of the system, except λ_0 and λ_Λ since their locations are fixed. The set of possible selections of λ defines $\mathcal{S}$, which is a subset of R^+. Therefore, s_t is defined to be a vector consisting of the current locations of λ_ls for $l = \{0, 1, 2, \cdots, \Lambda\}$.
- *Action space* $\mathcal{A}$: We design the RL algorithm in such a way that in every subsequent iteration only one agent, e.g. λ_l, can change its status. Thus,

$$a_t \in \{-1, 0, +1\}, \tag{18}$$

where $-1, 0$, and 1 represent decreasing the index of the agent in $\mathcal{S}$ by one, no change, and increasing the index of the agent in $\mathcal{S}$ by one, respectively. Here, we also apply the ϵ-greedy strategy [20], which can be defined as selecting the best action with probability $(1 - \epsilon_t)$ and a uniformly distributed random action with probability ϵ_t, which gives the search algorithm the possibility to explore the whole state space $\mathcal{S}$ without getting stuck into a local maximum. Additionally, it is important to note that any selected action a_t shall not cause any contradiction with the constraint defined in (17b).

- *Reward space* Ω: The reward function is defined as the empirical mean of the goodput that is achieved with the new state s_t, i.e.

$$\omega_t = \frac{1}{M}\sum_{m=1}^{M} C(\lambda_{L(\gamma_m)}) \triangleq G_{\text{emp}}^{M}, \tag{19}$$

where M represents the number of transmitted blocks with state s_t and yet is another design configuration of the RL model which will be discussed in the next section.

A. Q-Learning for Enhancing Goodput

The traditional approach in reinforcement learning involves a method known as Temporal Difference (TD) learning. This technique blends aspects of both Monte Carlo and dynamic programming. It is similar to Monte Carlo since TD learning acquires samples directly from the environment, and it is similar to dynamic programming since it refines its estimates based on both the current and previous assessments. One of the main TD learning methods is Q-learning which can be represented as an RL methodology allowing the agent to acquire the best strategy for navigating a specific environment [21]. This requires the agent to keep track of an approximation of the anticipated long-term discounted rewards for every possible state-action combination and then make choices to maximize these rewards.

In the Q-learning process, the agent iteratively updates its Q-table, which stores the expected cumulative rewards for each state-action pair. The optimal policy can be found by Bellman's optimality equation [21]

$$Q^*(s,a) = \mathrm{E}[\omega_{t+1} + \eta \max_{a'} Q^*(s_{t+1}, a') | s_t = s, a_t = a] \tag{20}$$

where η represents the discount factor which is required to bound the cumulative reward and $\max_{a'} Q^*(s_{t+1}, a')$ defines the best estimate for the next state s_{t+1}. (20) reveals that Q-learning requires the current state-action pair, the resulting reward, and the subsequent state. Thus, the updating process of the Q-table can be formulated as

$$Q(s_t, a_t) = (1-\alpha)Q(s_t, a_t) + \alpha(\omega_t + \eta \max_{a'} Q^*(s_{t+1}, a')), \tag{21}$$

where α is the learning rate.

The total number of possible s_ts in the current problem can be expressed as

$$|\mathcal{S}|!/((\Lambda+1)!(|\mathcal{S}| - \Lambda - 1)!), \tag{22}$$

where $|\cdot|$ represents the cardinality of the set. Given the potential for rapid growth of this number, constructing a comprehensive Q-table covering all possible s_t states becomes impractical. To address this challenge, we adopt a strategy where the algorithm treats each agent independently, thus it only needs the creation of distinct Q-tables for each agent. Additionally, given the variability in channel characteristics, the Q-table must encompass all feasible K values.

Consequently, the Q-learning table size for each agent is determined as $|\mathcal{K}||\mathcal{S}|$, where $\mathcal{K}$ is the set of all possible Rician-K factors. Notably, it remains possible to append these distinct Q-tables into a unified table with size

$$(\Lambda - 1)|\mathcal{K}||\mathcal{S}| + 1. \tag{23}$$

B. Algorithm Design

The proposed algorithm is implemented as follows

- Set M, α, η, and initialize the λ_l values for all agents.
- Initialize the Q-learning table with zeros. Set the ϵ values for all agents, where $\epsilon_1 = 0.5$ in our implementation.
- Start the loop by selecting an agent, i.e. λ_l, where at each iteration a different agent is selected.
- Select an action based on the ϵ-greedy algorithm.
- Update ϵ_t with respect to t, such that $\epsilon_{t+1} = \epsilon_t/\sqrt{t}$.
- After selecting a_t, update λ_l and s_t.
- Send the new r_l to the transmitter.
- Observe M number of transmissions, compute the reward ω_t according to (19), and update the Q-table using (21).

It is important to note that the proposed algorithm may not yield the optimal feedback scheme, which is due to the simplification of the Q-table size, as explained earlier, but it achieves a close approximation.

V. Performance Evaluation

Here, we first show the effect of M on the algorithm performance. For this purpose, we implement a Monte Carlo simulation where $\Lambda = 4$, $K = 10$dB, and $\mathcal{P} = 20$dB for $M = \{10^2, 10^3\}$ and show the average of ω_t at each iteration t with the variance with grey color around the average. Results are depicted in Fig. 3, where the long-term maximum achievable goodput value is also plotted as a dash-dotted line. The results demonstrate that the effect of M is significant for the design of the system. As can be seen from Fig. 3, the algorithm can reach the optimum value in both cases but faster, in terms of t, when $M = 10^3$. However, note that higher M values require more transmission at each iteration. On the other hand, in some cases, ω_t exceeds the upper limit due to its empirical nature.

Next, we focus on the overall performance of the proposed method, where we set $\Lambda = 4$, $\mathcal{P} = 20$dB, $N = 10^2$, and $M = 10^2$, and let K change from 0dB to 10dB then to 20dB. To see the overall performance, we again implement a Monte Carlo environment, from where the average ω_ts at each iteration t are obtained and depicted in Fig. 4. The long-term maximum achievable goodput values for each K are also plotted with dash-dotted lines. It is possible to see that the proposed method can track the change in channel statistics and adapt its feedback scheme so that it can approach the maximum achievable goodput values in every case. It is also important to highlight that, thanks to the RL-based learning approach, once the optimal feedback scheme for a particular Rician-K factor is determined, the transceivers can instantly adjust to the optimal scheme whenever the channel exhibits the same K value.

VI. Conclusions

In this study, we introduce a learning-driven system for goodput maximization with quantized feedback in wireless communication, designed to meet the requirements of URLLC. Our contributions include a novel Rician-K factor estimation technique that improves the adaptability of feedback strategies to changing channel conditions. Additionally, we employed RL to dynamically select and update feedback schemes, demonstrating the system's ability to maximize goodput under evolving channel conditions. The importance of dynamic feedback mechanisms is emphasized, which addresses the unique

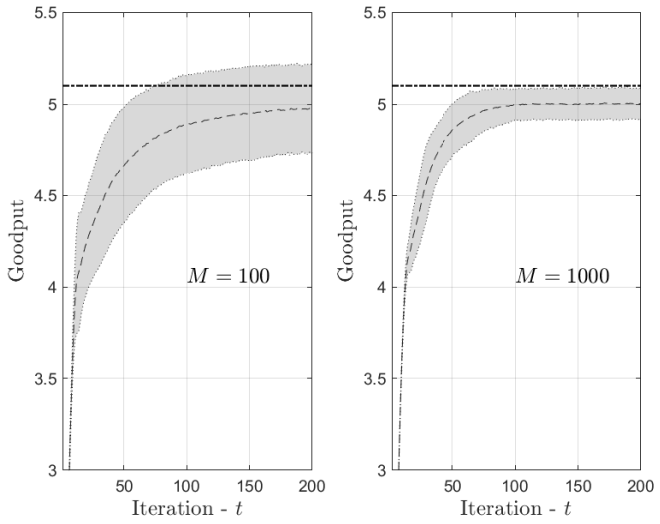

Figure 3. Mean and confidence region of ω_t with respect to iteration t for $M = \{100, 1000\}$ when $\Lambda = 4$, $K = 10$dB, and $\mathcal{P} = 20$dB. (— · —) The long-term average of the maximum achievable goodput. (- - -) Average of ω_t.

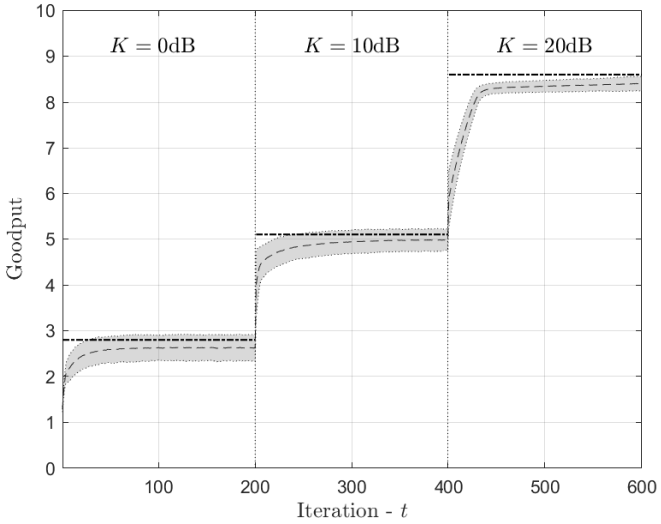

Figure 4. Performance of the proposed method with varying K. (— · —) Long-term average of the maximum achievable goodput. (- - -) Average of ω_t.

challenges posed by URLLC in next-generation wireless networks. Future research could extend the proposed framework to various other wireless communication scenarios.

REFERENCES

[1] H. B. Celebi, "Wireless transmission in future cyber-physical systems," PhD thesis, KTH Royal Institute of Technology, Stockholm, Sweden, 2021.

[2] F. Etemadi and H. Jafarkhani, "Joint source-channel coding for quasi-static fading channels with quantized feedback," in *2007 IEEE International Symposium on Information Theory*, 2007, pp. 2241–2245.

[3] T. T. Kim and M. Skoglund, "On the expected rate of slowly fading channels with quantized side information," *IEEE Transactions on Communications*, vol. 55, no. 4, pp. 820–829, 2007.

[4] H. B. Celebi and M. Skoglund, "Goodput maximization with quantized feedback in the finite blocklength regime for quasi-static channels," *IEEE Transactions on Communications*, vol. 70, no. 8, pp. 5071–5084, 2022.

[5] T.-K. Le, U. Salim, and F. Kaltenberger, "Feedback enhancements for semi-persistent downlink transmissions in ultra-reliable low-latency communication," in *European Conference on Networks and Communications*, 2020, pp. 286–290.

[6] S. AlMarshed, D. Triantafyllopoulou, and K. Moessner, "Deep learning-based estimator for fast HARQ feedback in URLLC," in *IEEE 32nd Annual International Symposium on Personal, Indoor and Mobile Radio Communications*, 2021, pp. 642–647.

[7] G. Pocovi, A. A. Esswie, and K. I. Pedersen, "Channel quality feedback enhancements for accurate URLLC link adaptation in 5G systems," in *IEEE 91st Vehicular Technology Conference*, 2020, pp. 1–6.

[8] H. B. Celebi, A. Pitarokoilis, and M. Skoglund, "A multi-objective optimization framework for URLLC with decoding complexity constraints," *IEEE Transactions on Wireless Communications*, vol. 21, no. 4, pp. 2786–2798, 2022.

[9] B. Makki and T. Eriksson, "On hybrid ARQ and quantized CSI feedback schemes in quasi-static fading channels," *IEEE Transactions on Communications*, vol. 60, no. 4, pp. 986–997, 2012.

[10] A. Abdi, C. Tepedelenlioglu, M. Kaveh, and G. Giannakis, "On the estimation of the k parameter for the rice fading distribution," *IEEE Communications Letters*, vol. 5, no. 3, pp. 92–94, 2001.

[11] H. B. Celebi, A. Pitarokoilis, and M. Skoglund, "Low-latency communication with computational complexity constraints," in *IEEE International Symposium on Wireless Communication Systems*, 2019, pp. 384–388.

[12] H. B. Celebi, A. Pitarokoilis, and M. Skoglund, "Latency and reliability trade-off with computational complexity constraints: OS decoders and generalizations," *IEEE Transactions on Communications*, vol. 69, no. 4, pp. 2080–2092, 2021.

[13] J.-M. Nicolas and F. Tupin, "A new parameterization for the rician distribution," *IEEE Geoscience and Remote Sensing Letters*, vol. 17, no. 11, pp. 2011–2015, 2020.

[14] S. O. Rice, "Mathematical analysis of random noise," *The Bell System Technical Journal*, vol. 23, no. 3, pp. 282–332, 1944.

[15] H. B. Celebi, A. Pitarokoilis, and M. Skoglund, "Training-assisted channel estimation for low-complexity squared-envelope receivers," in *IEEE 19th International Workshop on Signal Processing Advances in Wireless Communications*, 2018, pp. 1–5.

[16] M. Alymani *et al.*, "Rician k-factor estimation using deep learning," in *29th Wireless and Optical Communications Conference*, 2020, pp. 1–4.

[17] P.-Y. Hsu, I.-W. Yeh, C.-H. Tseng, and S.-J. Lee, "A boosting regression-based method to evaluate the vital essence in semiconductor industry performance," *IEEE Access*, vol. 8, pp. 156 208–156 218, 2020.

[18] D. Nielsen, "Tree boosting with XGBoost," M.S. thesis, Norwegian University of Science and Technology, Trondheim, Norway, 2016.

[19] D. T. Hoang, N. V. Huynh, D. N. Nguyen, E. Hossain, and D. Niyato, "Markov decision process and reinforcement learning," in *Deep Reinforcement Learning for Wireless Communications and Networking*. 2023, pp. 25–36.

[20] A. Masadeh, Z. Wang, and A. E. Kamal, "Reinforcement learning exploration algorithms for energy harvesting communications systems," in *IEEE International Conference on Communications*, 2018, pp. 1–6.

[21] B. Jang, M. Kim, G. Harerimana, and J. W. Kim, "Q-learning algorithms: A comprehensive classification and applications," *IEEE Access*, pp. 133 653–133 667, 2019.

Comparative Analysis of 130nm PDSOI and 28nm FDSOI Technologies for 5G Power Amplifier Applications

[1]Marcos L. Carneiro, [2]Tristan Lecocq, [3]Eric Kerhervé, [4]Magali de Matos, [5]Thierry Taris, [6]Jean-Marie Pham
[1]Postgraduate Program in Industrial and Systems Engineering, Pontifical Catholic University of Goiás, Goiânia, Brazil.
[1,2,3,4,5,6]University of Bordeaux, CNRS UMR 5218, Bordeaux INP, Talence, France.
e-mail: [1]mcarneiro@pucgoias.edu.br, [2]tristanlecocq@free.fr, [3]eric.kerherve@bordeaux-inp.fr, [4]magali.de-matos@u-bordeaux.fr, [5]thierry.taris@ims-bordeaux.fr, [6]jean-marie.pham@u-bordeaux.fr

***Abstract*— This paper analyzes 130 nm Partially Depleted (PD) Silicon-On-Insulator (SOI) and 28 nm Full Depleted (FD) SOI technologies and proposes the design of two Power Amplifiers (PAs) for 5G Narrow Band-Internet of Things (NB-IoT) applications. They were fabricated and measured, demonstrating the gain adjustment capability of FDSOI technology via back-gate voltage, allowing approximately 3.6 dB of gain adjustment. Both PAs consist of a gain stage (driver) and a power stage, using pseudo-differential and cascode topologies. The 28 nm PA includes an additional stacked transistor in the power stage to accommodate a higher drain bias voltage. Both PAs met the required performance parameters in post-layout simulations, achieving maximum Power-Added Efficiency (*PAEmax)* of 49% and 38.5%, gain of 36 dB and 34 dB and saturated Power (*Psat)* of 32 dBm and 28.8 dBm, respectively for 130 nm and 28 nm, placing them at the state-of-the art.**

Keywords- Power Amplifier; CMOS; 130 nm PDSOI; 28 nm FDSOI; 5G applications; Nb-IoT.

I. INTRODUCTION

The transition from 4G Long Term Evolution (LTE) to 5G has revolutionized the Internet of Things (IoT) with the advent of massive IoT, enabling the connection of numerous devices simultaneously. Narrow Band-Internet of Things (NB-IoT), a key 5G standard within Low-Power Wide-Area Networks (LPWAN), addresses the need for massive IoT by supporting battery-powered devices with extended lifespans and optimized installation costs. Operating on licensed 3GPP bands, NB-IoT offers higher data rates compared to unlicensed LPWAN technologies like LoRa and Sigfox. It achieves extensive coverage through transmission repetitions and increased signaling power, while its Single-Carrier Frequency Division Multiple Access (SC-FDMA) modulation reduces Peak-to-Average Power Ratio (PAPR), improving Power Amplifier (PA) efficiency and ensuring suitability for massive IoT applications [1].

Silicon-on-insulator (SOI) technology is pivotal for overcoming RF integration challenges in IoT circuits. Leveraging the high integration capabilities of Complementary Metal-Oxide-Semiconductor (CMOS), SOI reduces parasitic capacitances with a BOX layer, enhancing performance by over 20% [2]. While SOI improves reliability, energy efficiency, and reduces variability compared to bulk CMOS [3], NB-IoT's SC-FDMA modulation imposes strict PA design requirements, demanding linear operation and efficiency at low power. Advanced SOI technologies like Partially Depleted SOI (PDSOI) and Full Depleted SOI (FDSOI) provide tailored solutions, excelling in isolation and low-power scenarios, respectively [4].

This paper analyzes the 130 nm PDSOI and 28 nm FDSOI technologies and proposes the design of two PAs for the 5G NB-IoT applications (see Fig. 1). The gain and linearity adjustment capability via the back-gate voltage of FDSOI technology is demonstrated. Both circuits consist of PAs with a gain stage (driver) and a power stage, using pseudo-differential and cascode topologies.

Following, Section II compares 130 nm PDSOI and 28 nm FDSOI technologies, highlighting their components and PA design methodology. Section III presents post-layout simulation and measurement results, including performance analysis, gain tuning via back-gate voltage for the 28 nm PA, and a state-of-the-art comparison. Section IV concludes with findings and future research directions.

II. DESIGN METHODOLOGY

This design methodology section presents a study on technologies and the designed PAs. Details about the metal layers of the 130 nm FDSOI and 28 nm PDSOI technologies are presented, followed by comparing both technologies

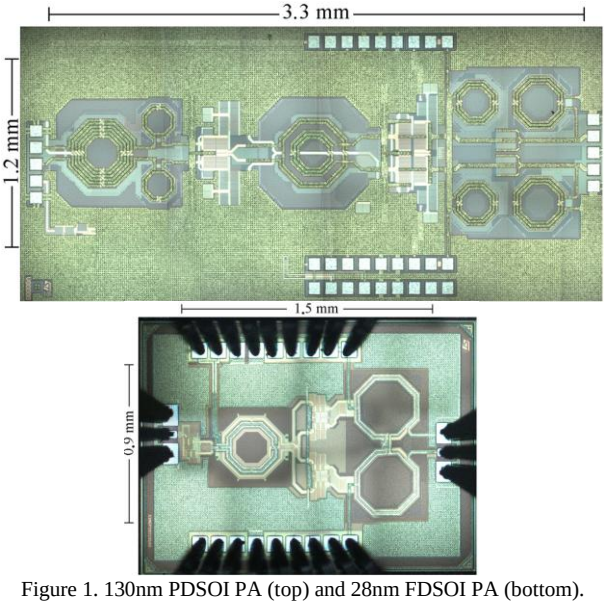

Figure 1. 130nm PDSOI PA (top) and 28nm FDSOI PA (bottom).

inductors, capacitors, and transistors. Based on this analysis, the following subsection provides details of the schematics of the two designed PAs, highlighting their similarities and differences.

A. *Evaluation of Passives and Transistors of SOI Technology*

Fig. 2 presents the metal layers of the 130 nm PDSOI and 28 nm FDSOI. The first observation concerns the difference in the number of available metal layers and their thickness. Indeed, the smaller the technology node, the higher the integration density, which also requires an increase in interconnection density. Several solutions are implemented to increase this density [5]. The rise in metal layers and the reduction of the minimum etching widths are the most common and easiest to apply. However, reducing the minimum etching width impacts the maximum thickness metal layers can have due to manufacturing processes. This consequently explains the reduction in the thickness of the metal layers in the 28 nm FDSOI.

Figs. 3 and 4 show an example of the inductor and capacitor performances for each technology, respectively. The comparison was made with inductors using an octagonal topology [6]. In 28 nm FDSOI, the inductors are designed on the three thick levels ALU-IB-IA (see Fig. 2) to reduce resistivity and increase the quality factor at low frequency. In 130 nm PDSOI, the two thick metal levels ALU-M4U (see Fig. 2) are used. For the same topology, the inductor achieves a quality factor *Q* of 28 at 2 GHz in 130 nm PDSOI, compared to 15 in 28 nm FDSOI. However, high-value inductors exhibit better high-frequency behavior in 28 nm FDSOI due to a higher self-resonant frequency, indicating lower parasitic capacitances. For capacitors, the quality factor at 2 GHz in the 130 nm technology is around 300 for a capacitance of 1.1 pF (see Fig. 4). For the 28 nm technology, the quality factor at 2 GHz is 40 for a capacitance of 0.88 pF. Indeed, the 28 nm technology has much thinner and more resistive metal layers than the 130 nm technology. On the other hand, the capacitors in 130 nm occupy larger silicon areas.

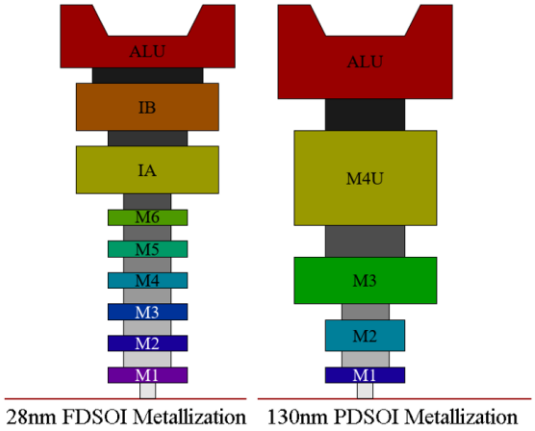

Figure 2. Metal layers of 28 nm FDSOI and 130 nm PDSOI technologies.

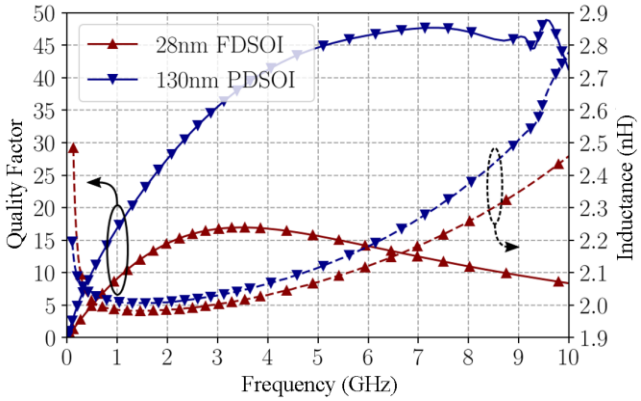

Figure 3. Comparison of inductances from 28 nm FDSOI and 130 nm PDSOI technologies.

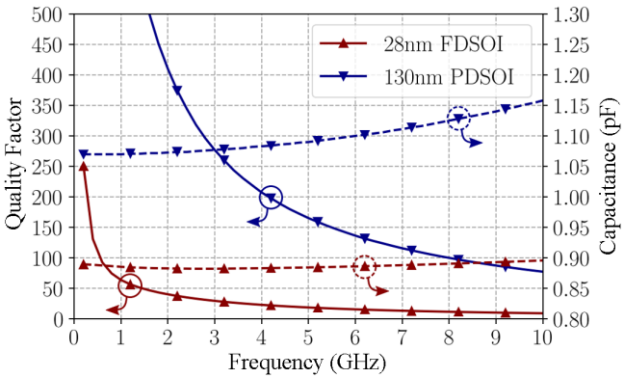

Figure 4. Comparison of capacitances in 28 nm FDSOI and 130 nm PDSOI technologies.

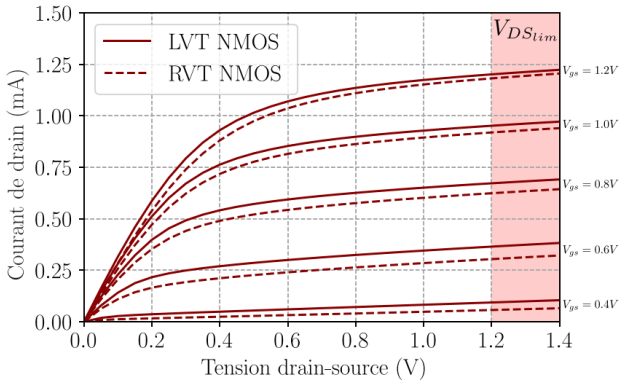

Figure 5. Output Transfer Characteristics Id(Vds) in 28 nm FDSOI.

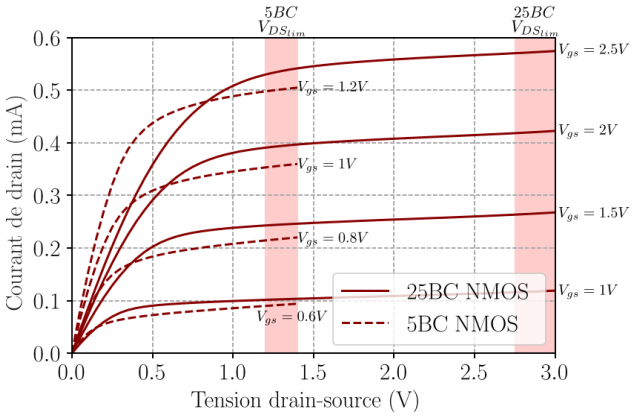

Figure 6. Output Transfer Characteristics Id(Vds) in 130 nm PDSOI.

Figs. 5 and 6 show NMOS transistors' output transfer characteristics for RF applications for PA design. The transistors from 28 nm FDSOI have a higher current density, reaching 1.2 mA at the maximum *Vgs* voltage, compared to 0.58 mA for the thick oxide transistor in 130 nm PDSOI. Additionally, the 28 nm transistors have lower threshold voltages, around 250 mV, compared to approximately 350 mV for the 130 nm transistors, enabling operation at lower voltages.

The 130 nm PDSOI technology offers better performance in terms of transistor quality in the saturation region. Indeed, the slopes *∂Id/∂Vds* in the saturation region are lower for the 130 nm PDSOI transistors than for the 28 nm FDSOI transistors. This also represents that the *gds* in 130nm are lower than in 28nm. The consequence is achieving more linear transistors for large-signal applications.

B. Power Amplifier Design Methodology

The two PA architectures were designed (see Figs. 7 and 8) based on the preliminary sizing of the transistors and the analysis of the presented passive components. Both architectures were designed to achieve comparable performance and NB-IoT restrictions in post-layout simulations. This allows for evaluating their fabricated circuit measurements to compare the two technologies and discuss their advantages and limitations concerning the target application.

Each circuit includes a driver stage with a single-ended input and pseudo-differential cascode topology at the output. Additionally, both circuits feature a pseudo-differential cascode power stage. The 28 nm design (see Fig. 7) employs a triple-cascode topology in its power stage to enable a supply voltage (*Vdd*) closer to the 130 nm technology, facilitating a fairer comparison. Both circuits were designed to achieve post-layout simulations (PLS) at the central frequency of 1.85 GHz, a bandwidth exceeding 400 MHz, a gain of 35 dB, a maximum Power-Added Efficiency (PAE_{max}) above 30%, and power back-off PAE (PAE_{PBO}) above 20%.

The 130 nm PDSOI PA, depicted in Fig. 8, incorporates a pseudo-differential cascode power stage alongside a pseudo-differential cascode driver setup. This configuration ensures a straightforward design and excellent performance tailored for NB-IoT applications. The design achieves higher output power by employing pseudo-differential architecture while minimizing constraints on the ground return path by suppressing even harmonics. Furthermore, the cascoded transistor arrangement enhances the amplifier's gain, allowing it to meet the 35 dB target specification. To ensure stability, given the high gain, neutralization capacitors (C_{neutro}) are incorporated. The matching networks are designed to enable broadband operation facilitated by a broadband matching transformer. In the 130nm technology, for the power stage, transistors were dimensioned with W_{total}=1200 µm and for the driver stage W_{total}=300 µm and the circuit was biased with *Vdd*=5V.

Fig. 7 shows the complete schematic of the PA in 28 nm FDSOI technology. Two power cells are combined in the

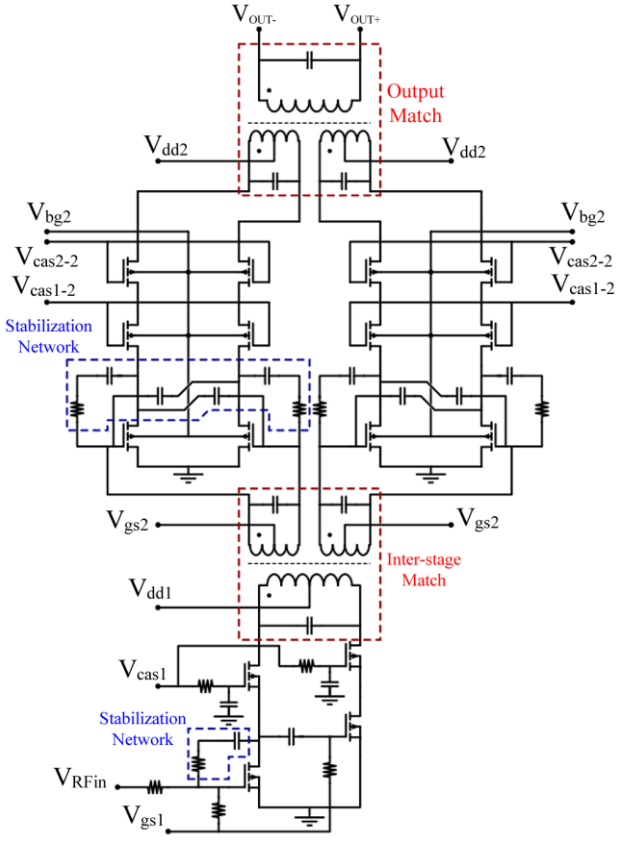

Figure 7. PA in 28 nm FDSOI technology schematic.

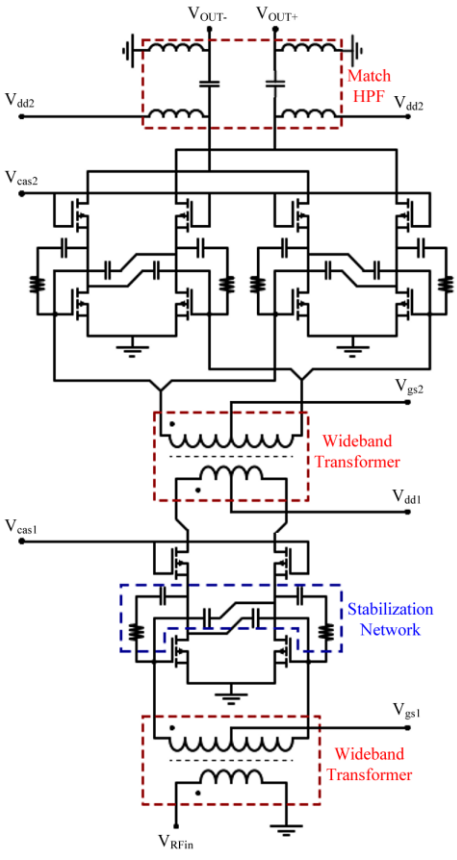

Figure 8. PA in 130 nm PDSOI technology schematic.

power stage to compensate for the technology's power limitations. The PA consists of two triple-stack power cells, enabling a total output power of 28 dBm. The output matching network uses a distributed active transformer (DAT) to optimize the load impedance at the output through series recombination. The inter-stage matching is designed around a 2-to-4 transformer, which performs impedance matching while distributing power across each power cell. Finally, the driver employs a cascode active balun topology, eliminating the need for a passive input balun. In the 28nm technology, the power stage used transistors with W_{total}=900 µm and for the driver stage W_{total}=225 µm, and the circuit was biased with *Vdd*=3V

This circuit explores the potential for improving output power using stacked architecture and back-gate biasing, aiming to meet the power requirements of NB-IoT applications. The back-gate voltage permits fine-tuning of the gain and linearity performance, as will be shown in the results section.

III. RESULTS AND DISCUSSIONS

A. Post-layout Simulation and Measurement Performance

Figs. 9 and 10 present the PA in 130 nm PDSOI and the PA in 28 nm FDSOI technologies S-parameters post-layout simulation (PLS) and measurements performance from 1 GHz to 3 GHz, respectively. The 130 nm PA presents an almost constant *S21* performance (between 35 dB and 39 dB) from 1.55 GHz to 2.4 GHz, an *S22* near -3 dB, and an *S11* less than to -5 dB in this frequency range. The 28 nm PA presents flatter behavior, with a maximum *S21* performance of 33 dB between 1.5 GHz and 1.8 GHz, *S22* less than -5 dB, and *S11* less than -15 dB.

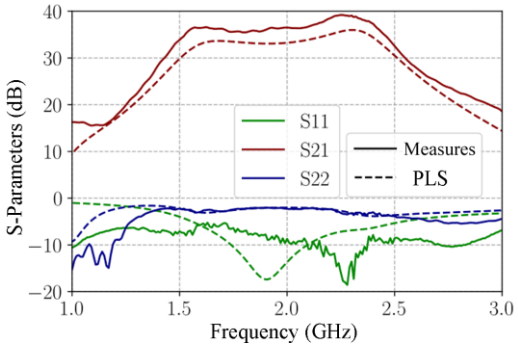

Figure 9. PA in 130nm PDSOI technology S-parameters post-layout simulation (PLS) and measurements performance.

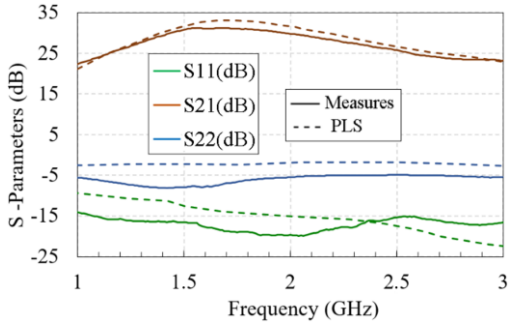

Figure 10. PA in 28nm FDSOI technology s-parameters post-layout simulation (PLS) and measurements performance.

Fig. 11 presents the PA in 130 nm PDSOI technology gain and PAE performances for post-layout simulation and measurements in the frequency of 1.85 GHz. The measured gain performance presents a class AB characteristic shape, with 34.5 dB in low power and a maximum of 36 dB; the maximum PAE reaches 48.5% at a P_{sat} of 31 dB in PLS and 38% in measurements at a P_{sat} of 28 dBm.

Fig. 12 presents the PA in 28 nm FDSOI technology gain and PAE performances for post-layout simulation in the frequency of 1.85 GHz. The gain performance achieves 33.26 dB in low power and a maximum of 34.72 dB; the maximum PAE reaches 38.5% at a P_{sat} of 28.5 dB. The transistors were optimized until the edge of stability parameters predicting that losses in further components would assure stability. However, the implemented circuit presented stability issues in high-output power.

B. Fine Tuning Gain with Back Gate Transistor Bias in 28nm FDSOI Technology

In CMOS SOI technology, access to the transistor's back-gate provides additional control over the device's characteristics that can be leveraged to modify key performance parameters of a PA, such as output power, gain, and PAE. Changing the back-gate bias (*Vbg*) effectively modulates the transistor's threshold voltage *Vth*. A lower threshold voltage can increase the transistor's current driving capability, which may increase the power output and, potentially, the gain, depending on the biasing conditions.

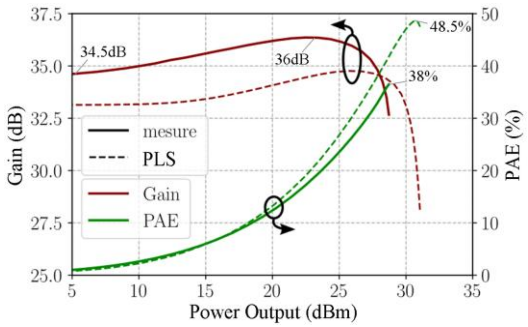

Figure 11. 130nm PA gain and PAE post-layout simulation and measured performances in 1.85 GHz.

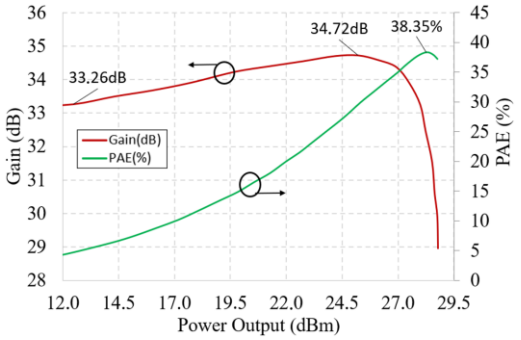

Figure 12. 28nm PA gain and PAE post-layout simulation performance in 1.85 GHz.

However, this also can lead to higher power consumption and decreased efficiency.

Fig. 13 presents the measured performance of gain versus P_{out} for the PA in 28 nm with three different levels of *Vbg* voltage. For *Vbg=2V*, the transistors are more biased for maximum conduction, resulting in the highest initial gain of 31.3 dB and a curve with the typical shape of a class AB PA, reaching 21.8 dBm of linear output power. A *Vbg=1V* offers a more balanced operation, with a lower initial gain (30.2 dB) but greater linearity up to higher output power levels (*OCP1*=22.2 dBm). Meanwhile, *Vbg=0V* shows the lowest gain (27.7 dB) due to reduced transistor conduction but the highest linear output power (*OCP1*=23.6 dBm).

These results demonstrate how the back-gate voltage in 28nm FDSOI technology can be leveraged to optimize amplifier performance according to specific requirements for gain and linearity.

C. 130nm and 28nm Power Amplifier Comparisons

This subsection compares the two PAs in size and performance. As seen earlier at the start of the results section, the PA implemented in 28 nm technology occupies an area corresponding to 34% of the area occupied by the PA in 130 nm technology.

Comparing Figs. 9 and 10, the PA based on 130 nm PDSOI technology outperforms the 28 nm FDSOI in S-parameters performance. The *S21* gain of the 130 nm PA remains around 35 dB in the central range (1.6 to 2.3 GHz), while the 28 nm PA reaches 30 dB only in the range between 1.5 and 1.9 GHz. However, the *S22* and *S11* of the 28 nm PA are more negative (below -5 dB and -15 dB, respectively), indicating better impedance matching at the input and output, with lower signal reflection.

PA gain (dB) and PAE (%) performances can be compared by Figs. 11 and 12. In PLS, the 130 nm PA achieves a higher maximum output power (~31 dBm) than the 28 nm PA (~28.5 dBm), making it more suitable for high-power applications. Considering the PLS performance, the 130 nm PA achieved a saturated output power of 31 dBm and the 28 nm PA achieved approximately 28.5 dBm, making the 130 nm technology more suitable for high-power applications, as expected. The 130 nm amplifier also provides slightly higher gain at lower output power levels. Furthermore, the 130 nm PA shows superior PAE performance in PLS, achieving a maximum of 48.5%, while the 28 nm PA achieves 38.35%. Comparing

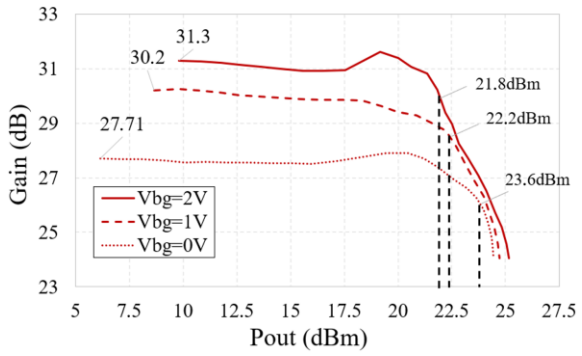

Figure 13. 28nm FDSOI PA gain versus P_{out} measured performances for 3 levels of back-gate voltage.

measurements, Fig. 11 shows that the 130 nm PA achieves a P_{sat} of 28.82 dBm and a P1dB of 27.29 dBm, while the 28 nm PA, in Fig. 13, reaches a P_{sat} of approximately 25.5 dBm and a P_{1dB} of 23.6 dBm.

Although the performance values of the circuit made with 130 nm technology are higher, the circuit in 28 nm technology allows for gain and linearity performance adjustment through back-gate voltage. This enables the choice to operate in either a high-gain mode or a high-linearity mode, depending on the communication requirements.

D. State-of-the-Art Analysis

A comparison with the state of the art is conducted to conclude the performance assessment of the PAs presented in this section. Table I summarizes the state-of-the-art PAs and the performance metrics of the PAs developed in this research.

Considering 5G and NB-IOT applications requiring modulations with high PAPR, the comparison was primarily made with promising topologies and techniques, such as Doherty, Envelope Tracking, and other high-efficiency classes.

It is observed that the two developed PAs outperform all PAs in Table I in terms of gain. Regarding *Psat*, the PA in 130 nm outperforms the works [5] [7] [8] [9] [10]. Regarding PAE, the PA in 130 nm outperforms the works [6] [8] [9] [10], and the PA in 28 nm outperforms the work [8].

Regarding output power, the developed PAs are promising, as they are being compared with Doherty PAs, which consist of two or more PAs in parallel. If double the power were considered for the presented PAs, they would be comparable to Doherty's maximum power-level topologies.

The 130nm PDSOI pseudo-differential PA demonstrates an overall performance superior to the 28nm FDSOI design. PAs [11] and [12] leverage off-chip passive components, which enhance performance due to significantly higher-quality factors than integrated passives. The PA architecture in [13] employs an envelope tracking technique, yielding a substantial improvement in PAE. Lastly, PA [14] is based on a switched amplifier architecture, enabling higher power density.

The PA designed in 28nm FDSOI is competitive with the state-of-the-art performance; however, the low-quality factor of integrated passives tends to reduce the maximum achievable PAE.

IV. CONCLUSION

This paper compares two PAs with some topological differences but similar application intents. Both consist of PAs with a gain stage (driver) and a power stage (PA), using differential and cascode topologies. The PA implemented in 28 nm technology presents a 3-stacked transistor in its power stage to allow for a higher drain bias voltage. This adjustment was deemed fair within the functional comparison, as the technology features thinner layers, necessitating such adaptations. The two employed technologies, 130 nm, and 28 nm, can produce PAs suited for the intended application.

This paper compares the passive and active elements of the two technologies, showing that the 130 nm PDSOI technology has much thicker layers than the 28 nm FDSOI

TABLE I - COMPARING WITH THE STATE-OF-ART

Ref.	Freq. (GHz)	Psat (dBm)	P1dB (dBm)	PAE max (%)	PAE 6dB (%)	Gain (dB)	Topology	Technology	Supply (V)
[15]	2.3	32.8	32	59	40	27.5	LDMOS Doherty	130nm SOI**	3.4
[16]	2.4	35.1	34	53		29.5	Doherty	130nm SOI	5
[5]	1.95	30.5	29.7	53	40	26.5	Doherty	180nm SOI	4
[7]	1.85	31.9	N/A	56.2		14.2	ET PA	180nm bulk	4
[6]	2.6	33.1	N/A	43.5	N/A	28.1	4-stack E/Fodd	45nm SOI	3
[8]	2.4	30.3	N/A	36.5	29.1	N/A	C-commutées	40nm Bulk	2.4
[9]	2.4	31.6	N/A	49.2		N/A	Digital Outphasing	45nm bulk	2.4
[10]	1.85	30.7	28.8	44.4	28	11	Quasi-Doherty	180nm SOI	3
PA 130*	**1.85**	**32**	**30**	**49**	**26.6**	**34**	**Cascode Classe-AB**	**130nm PDSOI**	**5**
PA 28*	**1.85**	**28.8**	**28.3**	**38.5**	**20.8**	**33**	**Triple stack Classe-AB**	**28nm FDSOI**	**3**

*PLS | **SOI with LDMOS option

technology, making it more suitable for power emission. However, the 28nm technology also enables this functionality while occupying three times less space, albeit at a considerably higher cost and with lower performance, given its primary orientation towards digital circuits.

The results indicate that the performance of the circuit fabricated in 130 nm technology is superior to that of the 28 nm circuit. The comparison between PLS and measurements also shows that the 130nm technology is more predictable and mature, as the measurements for the 28 nm circuit deviated further from the PLS predictions.

The 28 nm FDSOI technology enables fine-tuning of the PA's gain through back-gate voltage, thus providing additional operational freedom.

The developed PAs exhibit superior gain performance compared to the state-of-the-art. They are promising in power when used in efficiency-boosting topologies that combine multiple PAs to increase PAE at backoff and maximize output power.

For future research, it is suggested that we explore the use of these PAs in efficiency-enhancing topologies and power-combining strategies, Doherty and Envelope Tracking, facilitating comparisons with the state-of-the-art and contributing to the development of circuits for 5G and NB-IOT applications.

ACKNOWLEDGMENT

This study was financed in part by the project Beyond5 and by the *Coordenação de Aperfeiçoamento de Pessoal de Nível Superior - Brasil* (CAPES) - Finance Code 001.

REFERENCES

[1] K. Mekki, E. Bajic, F. Chaxel and F. Meyer, "Overview of Cellular LPWAN Technologies for IoT Deployment: Sigfox, LoRaWAN, and NB-IoT", IEEE International Conference on Pervasive Computing and Communications Workshops (PerCom Workshops), pp. 197–202, 2018.

[2] G. K. Celler and S. Cristoloveanu, "Frontiers of Silicon-on-Insulator", Journal of Applied Physics, vol. 93, pp. 4955–4978, 2003.

[3] H. Mendez, Silicon-on-Insulator, SOI Technology and Ecosystem, Emerging SOI Applications, April, 2009.

[4] A. Chen, Advances in Semiconductor Technologies: Selected Topics Beyond Conventional CMOS, Wiley-IEEE Press, 2023.

[5] IBM Corporation, BEOL Process Challenges - Emerging CMOS Technology at 5 nm and beyond, IEDM 2015 Short Course, Albany Nano Tech Center, NY, USA, 2015.

[6] B. Leite, Design and modeling of mm-wave integrated transformers in CMOS and BiCMOS technologies, University of Bordeaux, 2011BOR14359, PhD Thesis, 2011.

[7] T. Shen, W. Zhang, K. B. Yeap, J. Tan and P. Justison, "An Investigation of Dielectric Thickness Scaling on BEOL TDDB", IEEE International Reliability Physics Symposium, pp. 3A.2.1–3A.2.6. doi: 10.1109/IRPS.2015.7112698, 2015.

[8] A. Banerjee, L. Ding and R. Hezar, "A High Efficiency Multi-Mode Outphasing RF Power Amplifier With 31.6 dBm Peak Output Power in 45nm CMOS", IEEE Transactions on Circuits and Systems I : Regular Papers, t. 67, no 3, pp. 815-828, doi: 10.1109/TCSI.2019.2954068, 2020.

[9] P. Draxler and J. Hur, "A Multi-Band CMOS Doherty PA with Tunable Matching Network, IEEE MTT-S International Microwave Symposium (IMS)", pp. 944–946. doi: 10.1109/MWSYM.2017.8058742, 2017.

[10] Y. Eo and K. Lee, "High Efficiency 5GHz CMOS Power Amplifier with Adaptive Bias Control Circuit, IEEE Radio Frequency Integrated Circuits (RFIC) Systems", Digest of Papers, pp. 575–578. doi: 10.1109/RFIC.2004.1320686, 2004.

[11] A. Serhan, D. Parat and S. Gerardin, "A Reconfigurable SOI CMOS Doherty Power Amplifier Module for Broadband LTE High-Power User Equipment Applications", IEEE Radio Frequency Integrated Circuits Symposium (RFIC), pp. 79–82. doi: 10.1109/RFIC49505.2020.9218305, 2020.

[12] P. Reynier, A. Serhan, D. Parat and S. Gerardin, "A High-Power SOI-CMOS PA Module with Fan-Out Wafer-Level Packaging for 2.4 GHz Wi-Fi 6 Applications", IEEE Radio Frequency Integrated Circuits Symposium (RFIC), pp. 59–62, 2021.

[13] S. Jin, B. Park and K. Moon, "A Highly Efficient CMOS Envelope Tracking Power Amplifier Using All Bias Node Controls", IEEE Microwave and Wireless Components Letters, vol. 25, no. 8, pp. 517–519, 2015.

[14] M. Khorshidian and H. Krishnaswamy, "A Fully-Integrated 2.6GHz Stacked Switching Power Amplifier in 45nm SOI CMOS with >2W Output Power and 43.5% Efficiency", IEEE MTT-S International Microwave Symposium (IMS), pp. 323–326, 2019.

[15] Renesas Electronics, Semiconductor Reliability Handbook, R51ZZ0001EJ0250 Rev. 2.50, January, 2017.

[16] A. D. Pham, "Biasing Techniques for Linear Power Amplifiers", Ph.D. dissertation, Massachusetts Institute of Technology, May, 2002.